Article

Effects of L-Aspartic Acid on Cr(VI) Adsorption onto the Lepidocrocite with Different Exposed Facets: Batch Experiments and In Situ ATR-FTIR Analysis

Xiaofei Li [1],*, Tianfu Li [1], Xiaohu Jin [2], Yanfu Wei [3], Yanping Bao [1], Qian Yao [4], Fuhua Li [1], Weicheng Xu [1] and Xiaolian Wu [1]

1 School of Environmental and Chemical Engineering, Foshan University, Foshan 528000, China; 18437612672@163.com (T.L.)
2 National Demonstration Center for Environment and Planning, College of Environment and Planning, Henan University, Kaifeng 475004, China
3 National Observation and Research Station of Coastal Ecological Environments in Macao, Macao Environmental Research Institute, Macau University of Science and Technology, Taipa, Macao 999078, China
4 Guangdong Key Laboratory of Contaminated Environmental Management and Remediation, Guangdong Provincial Academy of Environmental Science, Guangzhou 510045, China
* Correspondence: xfli1103@fosu.edu.cn

Abstract: The adsorption of toxic metals onto iron oxides is a prevalent geochemical process in natural environments. Organic acids are known to modify the adsorption features of toxic ions through either competitive or cooperative effects. Nowadays, the toxic metal adsorption influenced by organic acids on iron oxides with varying facet exposures is not fully understood. This study explored how L-Aspartic acid (LA) influences Cr(VI) adsorption on two different exposure facets of lepidocrocite through batch adsorption experiments, in situ ATR-FTIR spectroscopy, and 2D-COS analysis. The results reveal that LA competes for available binding sites on lepidocrocite, consequently inhibiting the adsorption of Cr(VI). Rod-shaped lepidocrocite (R-LEP) owns more (001) facets and shows stronger Cr(VI) adsorption and LA competition than plate-like lepidocrocite (P-LEP), which mainly has (010) facets. The data for Cr(VI) uptake on both P-LEP and R-LEP within the effect of LA are well-fitted by the pseudo-second-order kinetics and the Freundlich isotherm model, suggesting chemical interaction as the dominant process for Cr(VI) coordination on lepidocrocite. Cr(VI) ions favor interaction with R-LEP over P-LEP, forming inner-sphere complexes on (001) facets. Concurrently, LA's carboxyl groups can compete for the active sites on the lepidocrocite surfaces, engaging in anion exchange with hydroxyl groups, and forming outer-sphere and inner-sphere structures. This competitive effect is particularly pronounced in the R-LEP system. The current findings are expected to broaden insights into how the exposed facets of lepidocrocite influence the fate of Cr(VI) in the organic acid coexistence environment.

Keywords: Cr(VI); L-Aspartic acid; adsorption; lepidocrocite; facet

1. Introduction

Hexavalent chromium (Cr(VI)) is the primary oxidation state of chromium in oxic environments [1]. Known for its toxicity and carcinogenicity, Cr(VI) poses a substantial threat to the health of both wildlife and humans [2,3]. Its environmental presence is largely linked to industrial activities, such as various industrial processes and the weathering of sulfidic ores and pyrite [4,5]. Cr(VI) is more mobile and bioavailable than trivalent chromium (Cr(III)) in biological systems, thereby amplifying its environmental risks [6]. Iron oxides, which are abundant in natural soils and sediments, are crucial in controlling the migration of Cr(VI) through interfacial interactions, such as adsorption, redox, and precipitation [7]. Consequently, elucidating how Cr(VI) interacts with iron oxide is imperative for mitigating environmental risks.

Lepidocrocite, with the chemical formula γ-FeO(OH), is a relatively unstable Fe-containing mineral frequently found in redoximorphic environments like sediments and paddy soils, playing a crucial role in regulating the fate of heavy metals (HMs) [8–10]. Moreover, lepidocrocite is recognized as a typical intermediate in the crystallographic transformation of precursor Fe oxides (ferrihydrite, Schwertmannite, etc.) [11–13]. This positioning enables lepidocrocite to serve as a bridging agent in controlling Fe cycling and trace element partitioning [14]. Therefore, investigating the surface reactivity of lepidocrocite through its interfacial interactions with heavy metals (HMs) holds significant environmental implications [8,15]. As well known, naturally formed lepidocrocite mainly consists of two typical morphologies, including plate- and rod-like shapes, presenting varying ratios of exposed facets [16–18]. These different morphologies correlate with differences in surface reactivity, such as adsorption performance, coordination structures, and interfacial electron transfer capability [8,19–21]. The plate-shaped lepidocrocite is primarily characterized by its (010) facet termination, which features a high density of bidentate hydroxyl groups (μ-OH), thereby supporting oxyanion adsorption [7,22–24]. Molybdenum(VI), for example, generates protonated binuclear monodentate complexes on the (010) facet of lepidocrocite [23]. Similarly, Otte et al. [24] identified doubly protonated MB complexes as the predominant species for As(V) on the same lepidocrocite facet. Rod-shaped lepidocrocite features a notably high percentage of exposed (001) facets, which have rich singly-coordinated hydroxyl sites that can form distinct coordination modes compared to those on the (010) lepidocrocite facet. Li et al. [8] observed that Cr(VI) engages in protonated monodentate binuclear (MB) coordination on the (010) facet and bidentate binuclear (BB) coordination on the (001) facet. Moreover, the increased presence of the (001) facet leads to improved adsorptive capacity for ions. Therefore, the adsorption behavior of trace elements on lepidocrocite is significantly determined by the exposed facets.

Contrary to simplified systems with a single toxic metal and mineral, real-world environments are more complex and contain multiple minerals, inorganic ions, dissolved organic matter, etc. [25,26]. Understanding competitive and cooperative interfacial processes with these coexisting substances is essential for accurately predicting adsorption behavior [7,27,28]. It is well established that organic acids significantly affect the mobility of HMs in natural environments, as they can compete with HMs for binding sites on iron oxide surfaces or form ternary complexes [15,29,30]. For example, under acidic conditions, oxalic acid outcompetes Cr(VI) for the exchangeable groups on lepidocrocite [31]. Furthermore, Li et al. [7] discovered that oxalic acid more readily reduced Cr(VI) adsorption on rod-shaped lepidocrocite compared to plate-like forms, a difference primarily due to the types of exposed facets. Therefore, the competitive adsorption behavior of HMs on iron oxide surfaces is also determined by the exposed facets. As well known, the amino acid-mineral surface interactions are of great interest to a wide range of geochemical topics and processes [32,33]. Numerous studies have mainly focused on the polymerization of amino acids (including glutamate, lysine, and aspartate) on mineral surfaces and their adsorption behavior in the presence of Ca^{2+}, Mg^{2+}, and PO_4^{2-} [25,34,35]. For example, Yang et al. [25] observed that phosphate competition substantially diminished aspartate adsorption capacity on the goethite surface. Conversely, aspartate had a negligible effect on phosphate adsorption, which was predominantly governed by nonprotonated bidentate, monoprotonated bidentate, and diprotonated monodentate complexes. However, limited knowledge is available regarding the interfacial interaction mechanism of Cr(VI) on lepidocrocite in competition with amino acids, especially concerning the in situ adsorption process.

This study primarily investigates the impacts of L-Aspartic acid (LA) on Cr(VI) adsorption onto two morphologically distinct forms of lepidocrocite, which expose different ratios of (001) to (010) facets. The objectives are: (1) to demonstrate Cr(VI) adsorption performance (including kinetics, isotherm, and pH effects) on these two different lepidocrocite when coexisting with L-Aspartic acid, (2) to reveal the dynamic interfacial interaction of Cr(VI) and L-Aspartic acid on the lepidocrocite surface at the molecular level, and (3) to further disclose the facet-dependent Cr(VI) and L-Aspartic acid co-adsorption mechanism on lepidocrocite.

The relevant findings are anticipated to shed new light on the roles of the lepidocrite facet in controlling the fate of Cr(VI) within the organic acid coexistence environment.

2. Materials and Methods

2.1. Synthesis of Two Morphological Lepidocrite

Two distinguishable morphologies of lepidocrite (LEP), plate-shaped (P-LEP) and rod-shaped (R-LEP), were synthesized following the procedures reported by [8,36]. For P-LEP synthesis, 3.98 g of unoxidized $FeCl_2 \cdot 4H_2O$ (Strem Chemicals, Inc., Newburyport, MA, USA) crystals (20 mM Fe) were dissolved in 300 mL of deionized water with 0.2 M NaCl (Macklin Biochemical Co., Ltd., Shanghai, China) and stirred. The solution's pH was adjusted to 6.3 with 1 M NaOH (Macklin Biochemical Co., Ltd., Shanghai, China), and the air was supplied at 200 mL·min^{-1}. The oxidation and hydrolysis of Fe ions proceeded until pH stabilization was achieved without further NaOH supplementation. For R-LEP, the synthesis procedure was similar but used 60 mM Fe(II) and 0.75 M NaCl. The mixture's pH was maintained at 6.7, and air was bubbled through at approximately 100 mL·min^{-1}. Both end-products underwent centrifugation, multiple washes with pure water, and 24 hours of freeze-drying. The obtained solids were then ground and passed through 200 meshes.

2.2. Macroscopic Adsorption Experiments

The simultaneous adsorption of L-Aspartic acid (LA, Macklin Biochemical Co., Ltd., Shanghai, China) and Cr(VI) (K_2CrO_4, Aladdin Biochemical Technology Co., Ltd., Shanghai, China) was investigated through macroscopic adsorption experiments. In these experiments, 0.02 g of lepidocrite was suspended in 20 mL of a 0.01 mM NaCl solution containing Cr(VI) and LA at varying concentrations. The reactions were carried out in 30 mL brown bottles under oxic conditions, which were sealed and shaken vigorously at 180 rpm and 25 °C in an orbital shaker to ensure thorough mixing.

Experiments for adsorption isotherms were performed with Cr(VI) concentrations varying between 20 to 200 μM, and LA at levels of 10 and 50 μM, while keeping the system pH constant at 5.0. To determine how pH influences adsorption, we investigated pH-dependent adsorption curves at pH values ranging from 4.0 to 8.0, each with a fixed 100 μM Cr(VI) and two different LA concentrations (10 and 50 μM). Additionally, the kinetics of adsorption were explored with initial Cr(VI) concentrations set at 100 μM and LA concentrations at 10 μM and 50 μM, under a pH of 5.0. Sampling intervals were predetermined, covering a duration from 0 to 2 h. Upon reaching equilibrium or at designated time intervals. The suspension (2 mL) was passed through a 0.22 μm filter to isolate the aqueous phase for subsequent measurement. The remaining suspension was poured into 50 mL brown bottles and spun at 8000 rpm for 10 min. The leftover solid was then cleaned with deionized water and vacuum freeze-dried. After drying, the solid particles were sieved through a 200-mesh screen and kept for subsequent measurements.

2.3. In Situ ATR-FTIR Experiments

The real-time ATR-FTIR studies were conducted on a Nicolet iS10 spectrometer (Thermo Fisher Scientific, Waltham, MA, USA), featuring a multi-bounce horizontal ATR unit and a flow cell system. The OMNIC software package, version 8.2, was used for managing data collection and analysis [37]. A ZnSe ATR crystal, oriented horizontally, was hidden beneath a lepidocrite layer by evaporating a suspension containing 2.4 mg of lepidocrite at a concentration of 2.0 g·L^{-1}. The pH level of the solution was adjusted by introducing 0.1 M HCl or 0.1 M NaOH with a peristaltic pump set at a flow rate of 500 μL·min^{-1}. ATR-FTIR spectra were captured at 25°C, scanning from 4000 to 600 cm^{-1} at a 4 cm^{-1} resolution with 125 scans.

Before conducting the adsorption studies, the lepidocrite sample was equilibrated with a 0.01 M NaCl solution, and its spectrum was recorded to serve as the reference background. For the ATR-FTIR experiments, concentrations of 50 μM LA and 100 μM Cr(VI) were used, with pH values set at 8.0, 7.0, 6.0, 5.0, and 4.0. Spectra collection continued

until successive scans showed no notable differences. Furthermore, it was verified that the lepidocrocite film remained intact throughout the adsorption experiments [38]. The ATR-FTIR spectra data were baseline-corrected before analysis [37].

2.4. Analytical Methods

X-ray powder diffraction (XRD, Bruker D8 Advance, Bremen, Germany) was used to confirm the synthesized lepidocrocite and the components of reacted solid samples. The measurements spanned from 10 to 80° in 2θ, with steps of 0.02°. SEM images (Merlin, ZEISS, Oberkochen, Germany) were applied to assess the morphologies of the two lepidocrocites. The specific surface areas of the two synthesized lepidocrocites were obtained from our previous study [8], which were determined using an AUTOSORB IQ analyzer from Quantchrome (Boynton Beach, FL, USA). The Cr(VI) concentrations were assessed by the 1,5-diphenylcarbazide (DPC) technique [39].

After baseline correction and smoothing, the ATR-FTIR data were further analyzed using Two-Dimensional Correlation Spectroscopy (2D-COS) with the 2D Shige software (version 1.3) [40]. For the synchronous map, the auto-peak is indicative of the variations in the intensity of a peak over time, whereas the cross-peak signifies the correlated response to temporal perturbations observed at two distinct bands. The positive cross-peak indicates a simultaneous increase or decrease in the intensities of the two bands, while a negative cross-peak shows that the intensities of the bands change in opposite directions. In the asynchronous spectra, the absence of auto-peaks indicates that there are no self-correlated signals. The asynchronous cross-peak indicates the presence of two uncorrelated bands, suggesting they stem from distinct surface complexes or varied molecular settings within a single complex [41].

3. Results and Discussions

3.1. Characterization of the Solid Samples

The XRD patterns' diffraction peaks were all successfully matched to the lepidocrocite (AMCSD 0020687) (Figure 1a,b) [7,8,42], confirming that the prepared solids corresponded to the crystalline phases of lepidocrocite and were free from any additional impurity phases. In addition, the co-adsorption of LA and Cr(VI) on the two lepidocrocite samples was further analyzed using XRD. As displayed in Figure S1, the diffraction peaks of the reacted samples were identical to those of pure lepidocrocite, suggesting that the presence of adsorbed LA and Cr(VI) did not cause any phase changes under the specified conditions. Therefore, the surface adsorption reaction of LA and Cr(VI) on LEP was the predominant interfacial process. Our previous investigation also showed that oxalic acid can inhibit Cr(VI) adsorption on lepidocrocite by competing for binding sites, with almost no effect on driving dissolution and recrystallization reactions [7].

The two morphological lepidocrocite samples were subsequently monitored through SEM images. As depicted in Figure 1c,d, the samples exhibited two distinct morphologies: plate- and rod-shaped particles denoted as P-LEP and R-LEP. As noted in previous studies, the R-LEP samples exhibited a notably higher abundance of the (001) facet in comparison to the P-LEP samples [8]. In contrast, P-LEP is chiefly distinguished by its (010) facet, with a minimal presence of the (001) facet [43]. Subsequently, the increased thickness of R-LEP suggests a higher proportion of (001) facets relative to (010) facets exposed on the lepidocrocite surface [16]. Furthermore, the reactivity on the lepidocrocite surface is affected by the distribution and density of the reactive sites it contains. On the perfect (010) facet of lepidocrocite, only surface bidentate hydroxyl groups are found, which are not effective for substitution with oxalic acid [9]. In contrast, the (001) facet of lepidocrocite consists of monodentate and bidentate hydroxyl groups [8,18], and the former groups serve as active sites and are favorable for the adsorption of organic acids [7,9]. Consequently, lepidocrocite variants with distinct exposed facets may display unique co-adsorption characteristics at the interface. Our previous study has shown that Cr(VI) adsorption on lepidocrocite (LEP)

is highly facet-dependent [8]. Consequently, we deduce that the adsorption of Cr(VI) on R-LEP and P-LEP exhibits different patterns when LA is also present.
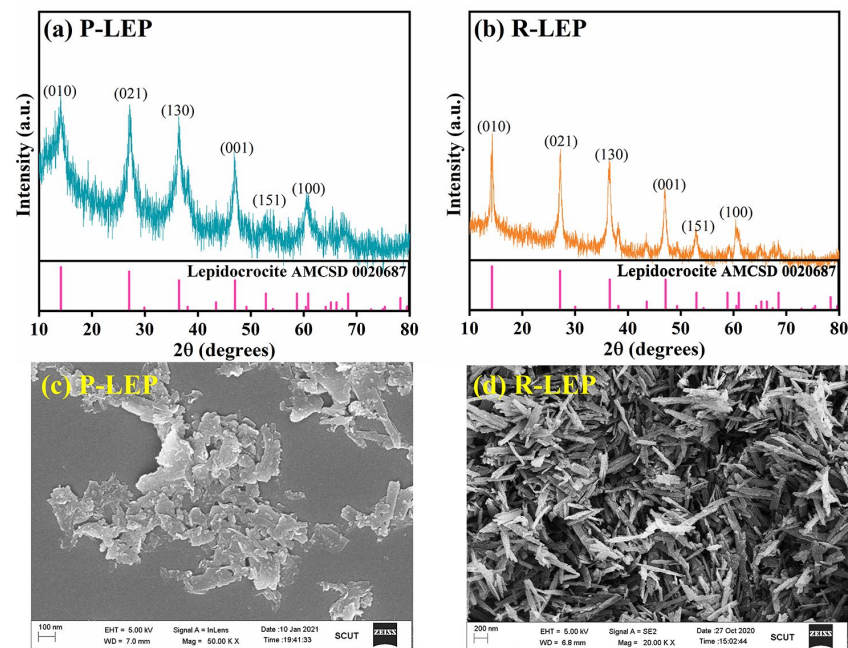

Figure 1. XRD patterns of P-LEP (**a**) and R-LEP (**b**), and their corresponding SEM images (**c**,**d**).

3.2. Cr(VI) Adsorption Kinetics in the Presence of LA

To elucidate the disparities in adsorption dynamics, the temporal progression of Cr(VI) uptake by R-LEP and P-LEP in the presence of LA was studied. The Cr(VI) uptake amounts were determined by normalizing the values concerning the specific surface area (P-LEP: 177 $m^2 \cdot g^{-1}$, R-LEP: 61 $m^2 \cdot g^{-1}$) [8]. As depicted in Figure 2a, at an initial LA concentration of 10 μM, the inhibitory effect on Cr(VI) adsorption was almost complete for both P-LEP and R-LEP. For the P-LEP system, the amount of Cr(VI) adsorbed declined from 0.029 $mg \cdot m^{-2}$ (5.15 $mg \cdot g^{-1}$) to 0.028 $mg \cdot m^{-2}$ (4.90 $mg \cdot g^{-1}$) with an increase in LA concentration from 10 to 50 μM, once equilibrium was reached. These values were significantly lower than the control group's value (0.065 $mg \cdot m^{-2}$) reported in our previous study [7]. This finding suggests that a competitive process takes place among these two anions on the P-LEP surface.
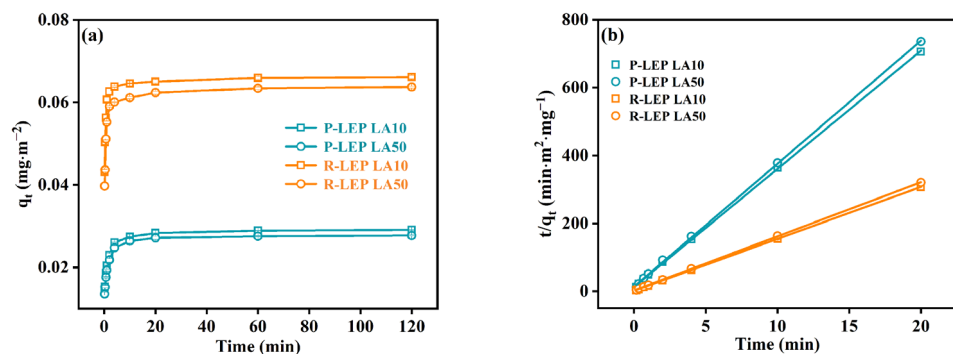

Figure 2. Time-dependent adsorption curves (**a**) and their kinetics plots (**b**) for Cr(VI) on P-LEP and R-LEP under the effects of LA.

In addition, R-LEP demonstrated superior adsorptive efficiency compared to P-LEP. As shown in Figure 2a, the saturation adsorption amount of Cr(VI) reached 0.065 $mg \cdot m^{-2}$ (3.97 $mg \cdot g^{-1}$) and 0.062 $mg \cdot m^{-2}$ (3.78 $mg \cdot g^{-1}$) under the influence of 10 μM and 50 μM LA, respectively. These values were considerably higher than those observed for P-LEP.

However, they were significantly lower than the control group's value ($0.137 \ mg \cdot m^{-2}$) reported in our previous study [7,8], also confirming that a strong competition occurred between LA and Cr(VI) on the R-LEP surface. The decreased amplitude of Cr(VI) adsorption on R-LEP under the impact of 10 µM LA compared to the CK was lower than that on P-LEP; this could be attributed to the greater exposure of the (001) facet on R-LEP, which provided rich binding sites for LA adsorption and reduced the inhibition effects on Cr(VI) adsorption. Interestingly, as the LA concentration continued to increase, the decrease in Cr(VI) adsorption amount on R-LEP was more pronounced compared to P-LEP. This enhanced sensitivity could be due to the greater involvement of LA in competing with Cr(VI) for the binding groups on the (001) facet. According to prior research [9], oxalate acid interacts with the (001) facet through an inner-sphere complex, in contrast to the outer-sphere complex it forms with the (010) facet. Consequently, it more readily competes with Cr(VI) for the binding groups on the (001) facet. Moreover, the adsorption data were effectively described by the pseudo-second-order kinetic model (Text S1) [44], which is illustrated in Figure 2b and Table S1. This suggests that the adsorption of Cr(VI) onto the two LEP surfaces under the effects of LA was primarily driven by chemical bonding [45].

3.3. Cr(VI) Adsorption Isotherms

The inherent Cr(VI) adsorption capacity on the two different morphological lepidocrocites at varying LA concentrations was explored using isotherm equations (Supplementary Section S2). Figure 3 indicates that the experimental data fit the Freundlich isotherm equations more closely than the Langmuir isotherm, suggesting a favorable scenario for multi-layer adsorption and chemical adsorption processes [46]. Regarding Cr(VI) maximum adsorption amount on R-LEP, it was $0.068 \ mg \cdot m^{-2}$ ($4.15 \ mg \cdot g^{-1}$) and $0.065 \ mg \cdot m^{-2}$ ($3.97 \ mg \cdot g^{-1}$) with the addition of 10 and 50 µM LA, respectively (Table S2). These values were significantly lower than those in the LA-free system ($0.137 \ mg \cdot m^{-2}$) [7], while being 2.24 and 2.25 times higher than those of P-LEP. The K_F values for the 10LA/P-LEP and 10LA/R-LEP systems were higher than those for 50LA/P-LEP and 50LA/R-LEP, confirming that Cr(VI) could be more readily adsorbed onto the LEP under the low concentration of LA. In our previous study, we estimated the proportions of the (010) and (001) facets on LEP to be 89.5% and 8.1% for P-LEP, and 67.6% and 30% for R-LEP, respectively [8]. This result also confirmed that competitive adsorption is facet-dependent. Furthermore, the adsorption of organic acids on the (010) facet predominantly occurs through outer-sphere complexes [7,9]. This process is primarily linked to the competitive adsorption that takes place on R-LEP, which has a higher concentration of (001) facet, as opposed to P-LEP, which is characterized by a predominance of (010) facet [8].

3.4. pH-Dependent Cr(VI) Adsorption onto LEP in the Presence of LA

Fluctuations in pH levels within the adsorption system can modify the adsorbent's surface charge and the forms of toxic metals and organic acids, resulting in varied adsorption behaviors for metals [47]. As depicted in Figure 4, there was a marked reduction in Cr(VI) adsorption capacity with increasing pH and LA levels, which implies that Cr(VI) adsorption is influenced by pH and is compromised by LA competition. Furthermore, the inhibitory effect for Cr(VI) uptake was more pronounced on R-LEP compared to P-LEP. The consequences are likely due to differences in the distribution of surface binding sites on the lepidocrocite. As noted in earlier studies, the bidentate µ-OH sites present on the (010) facet have a lower adsorption affinity for oxalate acid [9]. Nevertheless, such a facet is more conducive to the adsorption of oxyanions like chromate, molybdenum, and arsenate, forming monodentate structures [8,23,24]. In this study, it can be found that the inhibitory effects of LA on Cr(VI) adsorption exhibited a trend that first increased and then decreased as the pH continued to rise. These phenomena could be ascribed to the following reasons: (1) the speciation of LA around pH 4.0 primarily exists as a zwitterion with protonated NH_3^+ and γ-COOH [25]. At this condition, the Cr(VI) ions mainly existed as $HCrO_4^-$, which showed a high affinity to the Fe-OH active sites [34], behaving strongly competing with the protonated speciation of the LA for the surface sites. (2) Concurrently, the partial

deprotonation of γ-COOH of LA occurred as pH increases and may benefit from its interfacial interactions with the Fe-OH active sites, then exhibited a more significant effect in inhibiting the Cr(VI) adsorption. (3) As the pH continued to increase, the deprotonation of Fe-OH active sites at alkaline conditions could also diminish the chemical adsorption of LA onto the surface [7]. Meanwhile, the majority of the γ-COOH groups occurred deprotonation, leading to a more negative charge and resulting in the interfacial structures transformation from chemical bonding structures (inner-sphere γ-COOH complexation) to the physical adsorption speciation (outer-sphere NH_2 complexation) [25]. Under the pH range from 6.0 to 8.0, partial Cr(VI) ions could also interact with the iron oxide surface via the inner-sphere complexes at the pH range from 6.0 to 8.0 [1,44]. Therefore, the variations in the speciation of aqueous LA with pH increasing also determined the adsorption of Cr(VI) on LEP.
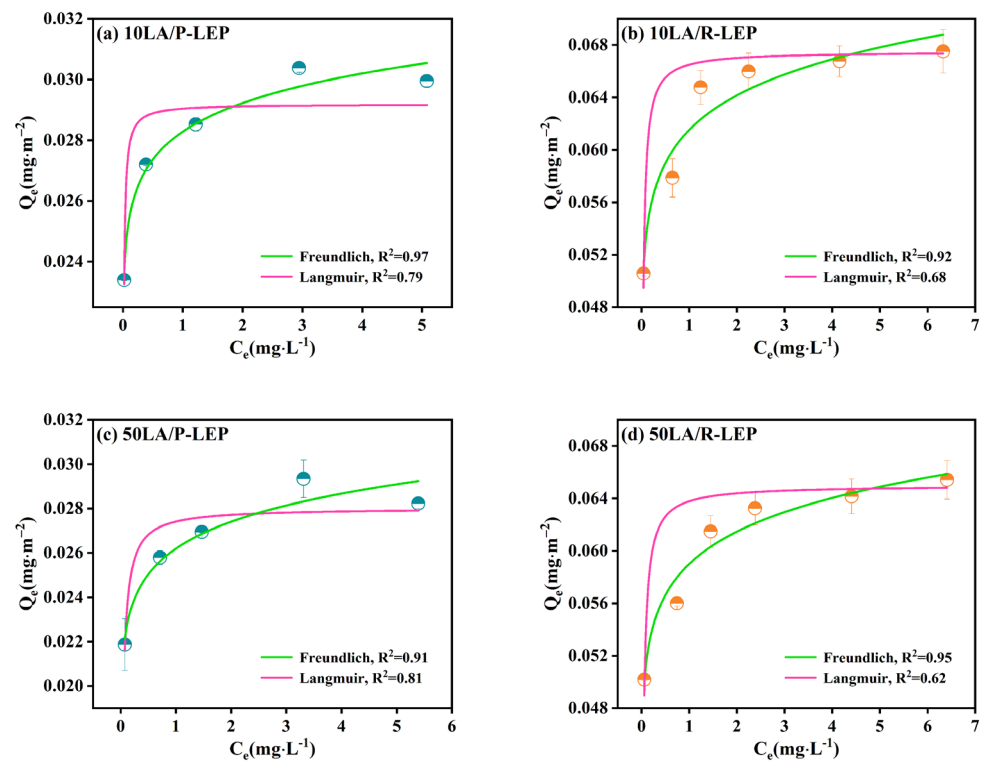

Figure 3. Isotherm analysis for Cr(VI) adsorption on P-LEP and R-LEP with Langmuir and Freundlich models at 10 μM (**a,c**) and 50 μM LA concentrations (**b,d**).
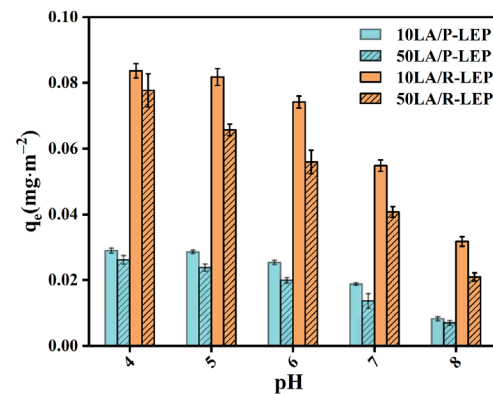

Figure 4. The influence of pH on Cr(VI) adsorption by P-LEP and R-LEP with varying LA concentrations.

3.5. Interfacial Dynamic Adsorption Process of Cr(VI) Under the Effects of LA

To gain insights into the dynamic simultaneous adsorption of Cr(VI) and LA on P-LEP and R-LEP, we employed in situ ATR-FTIR to probe their interfacial vibrational signals. It is crucial to first ascertain the speciation and vibrational characteristics of dissolved Cr(VI) and aqueous LA across a range of pH values. relevant information can be found in studies conducted by Johnston et al. [48] and Yang et al. [25]. Briefly, for dissolved Cr(VI), the peaks observed at 882 and 770 cm^{-1} correspond to the stretching modes of Cr-O and the asymmetric vibrations of the Cr-O-Cr bridge in $Cr_2O_7^{2-}$, respectively [49]. Meanwhile, the 901 cm^{-1} peak is indicative of the symmetric Cr-O stretching in $HCrO_4^-$ [37]. At pH 8.0, CrO_4^{2-} emerges as the predominant species in solution, which is evident from a distinct peak at 880 cm^{-1} [48]. For dissolved LA, there are three typical species: zwitterionic, monoanionic, and dianionic, which correspond to pH levels of 3.0, 6.0, and 11.0, respectively [25]. These species are primarily due to the (de)protonation of γ-COOH functional groups. ATR-FTIR analysis revealed that the $\delta_{as}(NH_3^+)$, $\delta_s(NH_3^+)$, and $\rho r(NH_3^+)$ modes are found at 1637, 1511, and 1272 cm^{-1}, respectively. The two bands at 1601 and 1396 cm^{-1} are attributed to the asymmetric and symmetric $\nu(\alpha\text{-COO}^-)$ vibrations, respectively [25]. As documented, the aspartate NH_2 group seldom engages in surface complexation on iron oxides, particularly at pH levels below 8.0 [50], whereas the -COOH group plays a significant role in the interaction [25]. Consequently, the observed spectral changes in this study are primarily attributed to the distinct interaction processes involving the -COOH group and the LEP surface.

Figure 5a,b display the ATR-FTIR spectroscopic analysis of the impact of varying pH on the simultaneous Cr(VI) and LA adsorption onto P-LEP and R-LEP. The spectra are categorized into three distinct regions: 1700–1100 cm^{-1} for the stretching vibrations of organic functional groups, 1100–980 cm^{-1} for Fe-OH vibrations [51], and 980–830 cm^{-1} for Cr-O vibrations [52]. The absorbance in the spectral region of 1700–1100 cm^{-1} increased significantly as the pH decreased from 8.0 to 4.0, suggesting substantial LA adsorption onto the LEP surface. The high spectral intensity, broader peaks, and well-defined shapes observed for LA adsorbed on R-LEP contrasted with those on P-LEP, suggesting the formation of outer-sphere and inner-sphere LA structures on R-LEP [25], which has a higher proportion of (001) facets. Concurrently, the region between 980–830 cm^{-1} exhibited a positive overlapping peak, with increasing absorbance as the pH decreased. This suggests that Cr(VI) can also be adsorbed onto both P-LEP and R-LEP surfaces under the influence of LA. Furthermore, the spectral position and shape of Cr-adsorbed R-LEP and P-LEP differed from those of dissolved Cr(VI) ions, indicating the formation of inner-sphere Cr(VI) complexes [1,37,48]. Meanwhile, the spectral region for Cr-adsorbed R-LEP exhibited more well-distinguishable than that for Cr-adsorbed P-LEP, proving a different ratio of surface inner-sphere Cr(VI) complexes formed on R-LEP and P-LEP [8]. As previously documented, Cr(VI) can coordinate with P-LEP and R-LEP by forming both binuclear monodentate and binuclear bidentate complexes. The binuclear monodentate Cr(VI) complex is the predominant structure on P-LEP, whereas the binuclear bidentate Cr(VI) complex is more abundant on R-LEP [8]. Additionally, the maximum peak position moved to higher wavenumbers as the pH decreased, indicating that Cr(VI) surface complexes might be transforming into more stable configurations. Interestingly, the region between 1100–980 cm^{-1} showed negative peaks, including a distinct peak at 1026 cm^{-1}, which represents the Fe-OH stretching vibration from the LEP surface. The absorbance of this peak decreased as the pH decreased, suggesting the release of hydroxyl groups from the P-LEP and R-LEP surfaces. This could be due to competition between LA and Cr(VI) for -OH groups on the LEP surface, leading to ligand exchange processes. Moreover, the amplitude decrease of the 1026 cm^{-1} peak was significantly greater in the R-LEP system than in P-LEP. This suggests that the active hydroxyl sites on R-LEP are more readily involved in ligand exchange with LA and Cr(VI) compared to those on P-LEP. This phenomenon can be attributed to the exposed (001) facet, which contains a higher concentration of singly-coordinated -OH [18]. Figure 5c,d display the kinetic curves for the three spectral regions, indicating a strong correlation between the

adsorption of LA and Cr(VI) and the release of surface-OH groups. Furthermore, R-LEP, with its increased availability of active sites on (001) facets, facilitates more competitive adsorption of Cr(VI) in the presence of LA, leading to a higher release of -OH groups.
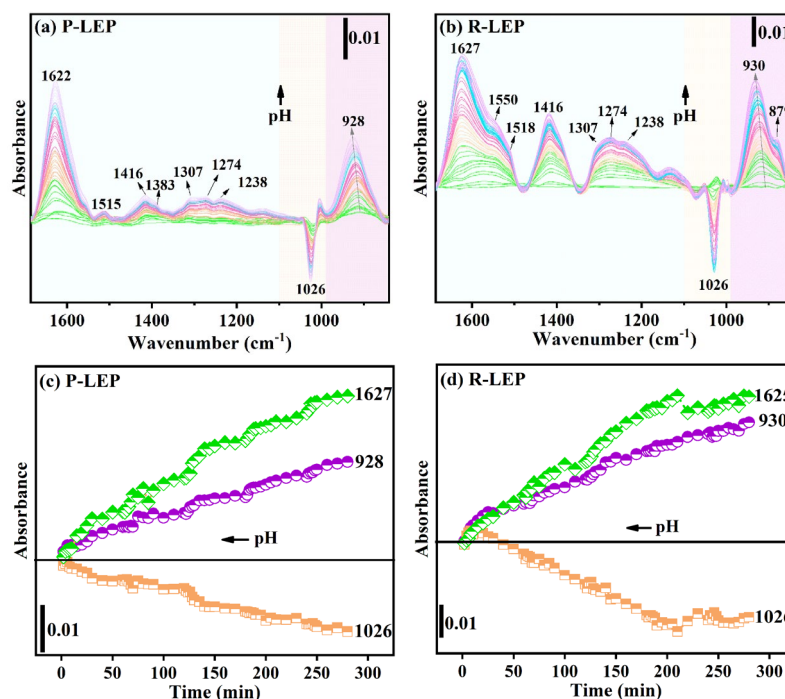

Figure 5. ATR-FTIR data collected as a function of time with flowing pH 8.0, 7.0, 6.0, 5.0, and 4.0 of LA and Cr(VI) on P-LEP (**a**) and R-LEP (**b**). Kinetic curves for the representative peaks of adsorbed LA and Cr(VI) and desorbed -OH groups for P-LEP (**c**) and R-LEP (**d**).

The 2D correlation contour plots were utilized to resolve the overlapping ATR-FTIR peaks [38], thereby improving our understanding of the interaction mechanisms between LA and Cr(VI) on the LEP surfaces. Figure 6a and Table S3 illustrate the synchronous correlation map for the LA-Cr/P-LEP systems, which features five diagonal peaks at 1622, 1416, 1274, 1026, and 928 cm^{-1}. These peaks indicate a significant change in spectral intensity associated with increasing reaction time and decreasing pH. Notably, the peaks at 1416 and 1274 cm^{-1} are less intense compared to the others. The peak at 1416 cm^{-1} was assigned to CH$_2$ scissoring [22]. Concurrently, the cross peaks at (1622, 1416), (1622, 1274), (1622, 928), (1416, 1274), (1416, 928), and (1274, 928) showed positive signals, indicating a similar trend in spectral intensity changes. In contrast, the negative cross peaks at (1622, 1026), (1416, 1026), (1274, 1026), and (1026, 928) suggest that the peak at 1026 cm^{-1} behaves differently, confirming distinct interfacial reactions, such as adsorption and desorption processes. In the asynchronous correlation map (Figure 6c and Table S4), the peak pairs at (1622, 1026), (1416, 1026), (1274, 1026), and (1026, 928) exhibited negative signals, mirroring the features observed in the synchronous correlation map. This consistency indicates that the peak at 1026 cm^{-1} is distinct and does not overlap with other peaks. As mentioned above, this peak is confirmed to be associated with the vibration of hydroxyl groups on the LEP surface. Concurrently, the peak pair at (1274, 928) exhibited a positive signal, which could be ascribed to the different vibrational sources among these two peaks. The former is assigned to the symmetric vibration of C-O, while the latter is attributed to the Cr-O vibration [9,37]. Additionally, the peak pairs, including (1612, 1274), (1622, 1378), and (1622, 1515), were also found in the synchronous correlation map. The peaks at 1515 and 1274 cm^{-1} are indicative of inner-sphere complexes involving carboxyl groups. The peak at 1612 cm^{-1}, corresponding to the asymmetric stretch of the COO$^-$ group, and the peak at 1378 cm^{-1}, associated with the symmetric stretch, are likely attributed to outer-sphere surface coordination on P-LEP. These observations are consistent with

the spectral characteristics of carboxyl groups in various coordination environments as reported in the literature [25,53]. These frequencies fall within the range of asymmetric stretching frequencies for aqueous carboxylates, which are typically found between 1540 and 1650 cm^{-1}, and symmetric stretching frequencies, which are found between 1300 and 1420 cm^{-1} [54]. In addition, it is observed that the maximum peak position at high pH is relatively lower than that at acidic conditions (Figure 5a,b), suggesting the formation of different complexes. Previous studies illustrated that the carboxyl group coordination modes change from outer-sphere to inner-sphere structures with pH decreasing, causing the corresponding peak to shift to the higher wavenumber [9,25]. Additionally, the 928 cm^{-1} peak is associated with the vibrational stretching of Cr-O bonds, indicating the formation of inner-sphere complexes as reported previously [1].
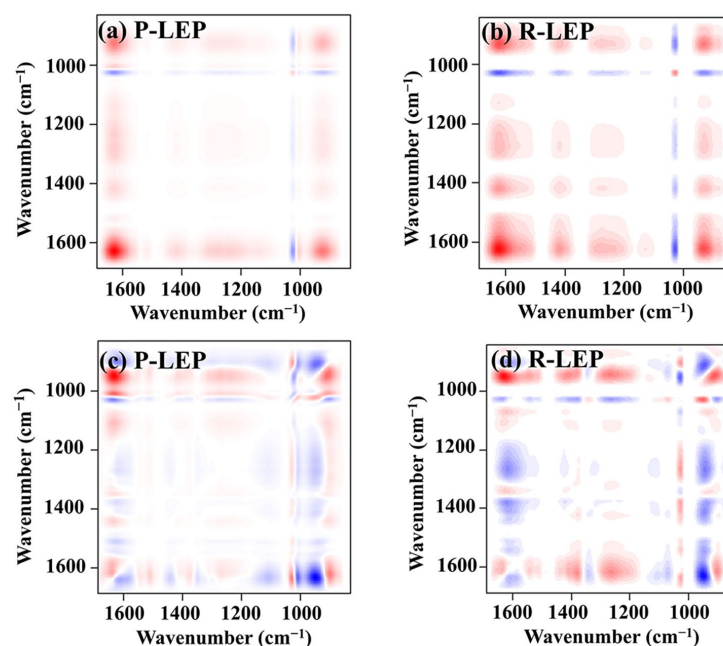

Figure 6. Synchronous contour plots for LA and Cr(VI) adsorbed onto P-LEP (**a**) and R-LEP (**b**) across varying pH levels, with corresponding asynchronous plots (**c,d**).

For the R-LEP, the synchronous correlation map (Figure 6b and Table S5) revealed six distinct diagonal peaks at 1627, 1550, 1416, 1274, 1026, and 930 cm^{-1}. Notably, the peak at 1550 cm^{-1}, corresponding to the asymmetric stretching vibration of COO$^-$ (v_{as}(COO$^-$)), was more pronounced than in the LA-Cr/P-LEP system's map, suggesting a greater interaction between LA and R-LEP via the carboxyl groups. This phenomenon is attributed to the higher exposure ratio of the (001) facet on R-LEP [7]. The signal change trends for the other peaks were similar to those observed in the LA-Cr/P-LEP systems. As seen in the asynchronous correlation map (Figure 6d) and Table S6, the negative peaks observed at (1602, 1550) and (1602, 1385) suggest that these three peaks might be associated with the stretching vibrations of the carboxyl groups, and are identified as part of outer-sphere complexes [25]. Meanwhile, the peak at 1602 cm^{-1} shifted significantly to a higher wavenumber at 1627 cm^{-1} with pH decreasing, which might be attributed to the strong interaction between LA and the R-LEP surface [51]. In addition, the peak pair at (1602, 1518) presented a negative signal, which cannot be observed in the synchronous correlation map. We concluded that these two peaks originated from different surface complexes, and the peak at 1518 cm^{-1} was assigned to the bidentate binding from the carboxyl groups [25,51]. The peak pair at (1274, 1026) showed a negative signal, confirming that the 1026 cm^{-1} peak originates from the vibration of surface Fe-OH complex structures. In summary, we conclude that the interfacial reactions involve three main processes: (1) LA interacts with LEP via carboxyl group coordination, forming both outer-sphere and inner-sphere structures;

(2) Cr(VI) adsorption on LEP, primarily through the formation of inner-sphere structures, including binuclear bidentate and monodentate structures; (3) competition between LA and Cr(VI) for surface hydroxyl groups, leading to ligand exchange processes.

4. Conclusions

This research illuminated the influence of LA on the adsorption of Cr(VI) by two types of lepidocrocite featuring distinct exposed facets. LA was identified as a competitor for the lepidocrocite surface active sites, thereby inhibiting the adsorption of Cr(VI). The dominant conclusions were summarized as follows:

- The competitive adsorption processes were found to be facet-dependent. Specifically, the rod-shaped lepidocrocite (R-LEP), which possesses a higher ratio of (001) facet, exhibits greater efficacy in Cr(VI) adsorption and resistance to LA competition compared to plate-shaped lepidocrocite (P-LEP), which is primarily composed of (010) facet.
- Cr(VI) interacts with the LEP surface under the influence of LA through a chemical reaction. The inner-sphere Cr(VI) complexation is more favored with R-LEP compared to P-LEP, demonstrating that more (001) facets provide more monodentate binding sites (-OH) for the competitive adsorption between Cr(VI) and LA.
- In addition, LA adsorbs onto LEP through the coordination of its carboxyl groups, forming inner-sphere and outer-sphere structures. The presence of inner-sphere LA complexes, which are primarily associated with the exposed (001) facet. The ligand exchange reaction with the hydroxyl groups on LEP appears to be the predominant interaction mechanism.

The findings shed light on the impact of lepidocrocite's exposed facets and coexisting substances on Cr(VI) migration in complex environments.

Author Contributions: X.L.: writing—original draft, conceptualization, funding acquisition, supervision; T.L.: investigation, data curation, methodology, writing—review and editing; X.J.: investigation, visualization, writing—review and editing; Y.W.: formal analysis, writing—review and editing; Y.B.: visualization, writing—review and editing; Q.Y.: software, writing—review and editing; F.L.: writing—review and editing; W.X.: writing–review and editing; X.W.: writing—review and editing. All authors have read and agreed to the published version of the manuscript.

Data Availability Statement: All relevant data has been included in the article.

Conflicts of Interest: The authors declare no conflict of interest.

References

1. Johnston, C.P.; Chrysochoou, M. Investigation of chromate coordination on ferrihydrite by in situ ATR-FTIR spectroscopy and theoretical frequency calculations. *Environ. Sci. Technol.* **2012**, *46*, 5851–5858. [CrossRef]
2. Qi, T.Y.; Zhang, S.; Zhang, J.Z.; Li, T.; Xing, L.; Fang, Z.M.; An, S.L.; Xu, Z.F.; Xiao, H.N.; Wang, L.D. In situ reconstruction of active catalysis sites triggered by chromium immobilization for sulfite oxidation. *Environ. Sci. Technol.* **2023**, *57*, 3905–3916. [CrossRef]

3. Kebir, M.; Tahraoui, H.; Chabani, M.; Trari, M.; Noureddine, N.; Assadi, A.A.; Amrane, A.; Ben Hamadi, N.; Khezami, L. Water cleaning by a continuous fixed-bed column for Cr(VI) eco-adsorption with green adsorbent-based biomass: An experimental modeling study. *Processes* **2023**, *11*, 363. [CrossRef]

4. Xie, Y.Y.; Ye, H.; Wen, Z.; Dang, Z.; Lu, G.N. Sulfide-induced repartition of chromium associated with schwertmannite in acid mine drainage: Impacts and mechanisms. *Sci. Total. Environ.* **2022**, *848*, 157863. [CrossRef] [PubMed]

5. Zhao, Q.; Yang, B.B.; Ren, H.W.; Chen, S.H.; Luo, C.H.; Li, Q.D.; Yang, W.; Yan, K.P. Removal of Cr(VI) from aqueous systems using Fe-P slag as a reducing agent. *Hydrometallurgy* **2022**, *211*, 105875. [CrossRef]

6. Chattopadhyay, B.; Utpal, S.; Mukhopadhyay, S.K. Mobility and bioavailability of chromium in the environment: Physico-chemical and microbial oxidation of Cr (III) to Cr (VI). *J. Appl. Sci. Environ.* **2010**, *14*, 97–101. [CrossRef]

7. Li, X.F.; Guo, C.L.; Pillai, S.C.; Jin, X.H.; Yao, Q.; Bao, Y.P.; Jiang, X.D.; Lu, G.N.; Wang, H.L.; Dang, Z. Facet-dependent competitive adsorption mechanisms of chromate and oxalic acid on γ-FeO(OH) nanocrystals. *Langmuir* **2023**, *39*, 14539–14549. [CrossRef]

8. Li, X.F.; Guo, C.L.; Jin, X.H.; Yao, Q.; Liu, Q.Q.; Zhang, L.J.; Lu, G.N.; Reinfelder, J.R.; Huang, W.L.; Dang, Z. Molecular-scale study of Cr(VI) adsorption onto lepidocrocite facets by EXAFS, in situ ATR-FTIR, theoretical frequency calculations and DFT+U techniques. *Environ. Sci. Nano* **2022**, *9*, 568–581. [CrossRef]

9. Borowski, S.C.; Biswakarma, J.; Kang, K.; Schenkeveld, W.D.C.; Hering, J.G.; Kubicki, J.D.; Kraemer, S.M.; Hug, S.J. Structure and reactivity of oxalate surface complexes on lepidocrocite derived from infrared spectroscopy, DFT-calculations, adsorption, dissolution and photochemical experiments. *Geochim. Cosmochim. Acta* **2018**, *226*, 244–262. [CrossRef]

10. Liao, S.; Wang, X.M.; Yin, H.; Post, J.E.; Feng, X.H. Effects of Al substitution on local structure and morphology of lepidocrocite and its phosphate adsorption kinetics. *Geochim. Cosmochim. Acta* **2020**, *276*, 109–121. [CrossRef]

11. Chen, C.M.; Kukkadapu, R.; Sparks, D.L. Influence of coprecipitated organic matter on $Fe^{2+}_{(aq)}$-catalyzed transformation of ferrihydrite: Implications for carbon dynamics. *Environ. Sci. Technol.* **2015**, *49*, 10927–10936. [CrossRef] [PubMed]

12. Schoepfer, V.A.; Burton, E.D.; Johnston, S.G. Contrasting effects of phosphate on the rapid transformation of schwertmannite to Fe(III) (oxy)hydroxides at near-neutral pH. *Geoderma* **2019**, *340*, 115–123. [CrossRef]

13. Jin, X.H.; Li, X.F.; Guo, C.L.; Jiang, M.G.; Yao, Q.; Lu, G.N.; Dang, Z. Fate of oxalic-acid-intervened arsenic during Fe(II)-induced transformation of As(V)-bearing jarosite. *Sci. Total. Environ.* **2020**, *719*, 137311. [CrossRef] [PubMed]

14. Jin, X.H.; Guo, C.L.; Tao, X.Q.; Li, X.F.; Xie, Y.Y.; Dang, Z.; Lu, G.N. Divergent redistribution behavior of divalent metal cations associated with Fe(II)-mediated jarosite phase transformation. *Environ. Pollut.* **2024**, *350*, 124004. [CrossRef]

15. Cao, Q.Q.; Guo, C.L.; Ren, M.H.; Li, X.F.; Xu, Z.R.; Wang, C.P.; Lu, G.N.; Dang, Z. Influence of tartaric acid on the electron transfer between oxyanions and lepidocrocite. *J. Hazard. Mater.* **2024**, *476*, 135082. [CrossRef]

16. Kozin, P.A.; Salazar-Alvarez, G.; Boily, J.F. Oriented aggregation of lepidocrocite and impact on surface charge development. *Langmuir* **2014**, *30*, 9017–9021. [CrossRef]

17. Paikaray, S.; Schröder, C.; Peiffer, S. Schwertmannite stability in anoxic Fe(II)-rich aqueous solution. *Geochim. Cosmochim. Acta* **2017**, *217*, 292–305. [CrossRef]

18. Ding, X.; Song, X.; Boily, J.F. Identification of fluoride and phosphate binding sites at FeOOH surfaces. *J. Phys. Chem. C* **2012**, *116*, 21939–21947. [CrossRef]

19. Hunge, Y.M.; Yadav, A.A.; Kang, S.W.; Kim, H.; Fujishima, A.; Terashima, C. Nanoflakes-like nickel cobaltite as active electrode material for 4-nitrophenol reduction and supercapacitor applications. *J. Hazard. Mater.* **2021**, *419*, 126453. [CrossRef]

20. Hunge, Y.M.; Yadav, A.A.; Kang, S.-W.; Kim, H. Facile synthesis of multitasking composite of Silver nanoparticle with Zinc oxide for 4-nitrophenol reduction, photocatalytic hydrogen production, and 4-chlorophenol degradation. *J. Alloys Compd.* **2022**, *928*, 167133. [CrossRef]

21. Yadav, A.A.; Hunge, Y.M.; Majumder, S.; Mourad, A.H.I.; Islam, M.M.; Sakurai, T.; Kang, S.W. Multiplicative rGO/Cu-BDC MOF for 4-nitrophenol reduction and supercapacitor applications. *J. Colloid Interface Sci.* **2025**, *677*, 161–170. [CrossRef]

22. Das, S.; Hendry, M.J.; Essilfie-Dughan, J.A. Adsorption of selenate onto ferrihydrite, goethite, and lepidocrocite under neutral pH conditions. *Appl. Geochem.* **2013**, *77*, 185–193. [CrossRef]

23. Davantès, A.; Costa, D.; Lefèvre, G. Molybdenum(VI) adsorption onto lepidocrocite (γ-FeOOH): In situ vibrational spectroscopy and DFT+U theoretical study. *J. Phys. Chem. C* **2016**, *120*, 11871–11881. [CrossRef]

24. Otte, K.; Schmahl, W.W.; Pentcheva, R. DFT+U study of arsenate adsorption on FeOOH surfaces: Evidence for competing binding mechanisms. *J. Phys. Chem. C* **2013**, *117*, 15571–15582. [CrossRef]

25. Yang, Y.L.; Wang, S.R.; Xu, Y.S.; Zheng, B.H.; Liu, J.Y. Molecular-scale study of aspartate adsorption on goethite and competition with phosphate. *Environ. Sci. Technol.* **2016**, *50*, 2938–2945. [CrossRef] [PubMed]

26. Meng, X.Q.; Wang, X.M.; Zhang, C.M.; Yan, S.; Zheng, G.Y.; Zhou, L.X. Co-adsorption of As(III) and phenanthrene by schwertmannite and Fenton-like regeneration of spent schwertmannite to realize phenanthrene degradation and As(III) oxidation. *Environ. Res.* **2021**, *195*, 110855. [CrossRef]

27. Flynn, E.D.; Catalano, J.G. Competitive and cooperative effects during nickel adsorption to iron oxides in the presence of oxalate. *Environ. Sci. Technol.* **2017**, *51*, 9792–9799. [CrossRef] [PubMed]

28. Situm, A.; Rahman, M.A.; Allen, N.; Kabengi, N.; Al-Abadleh, H.A. ATR-FTIR and flow microcalorimetry studies on the initial binding kinetics of arsenicals at the organic–hematite interface. *J. Phys. Chem. A* **2017**, *121*, 5569–5579. [CrossRef]

29. Mesuere, K.; Fish, W. Chromate and oxalate adsorption on goethite. 2. Surface complexation modeling of competitive adsorption. *Environ. Sci. Technol.* **1992**, *26*, 2365–2370. [CrossRef]

30. Yao, W.B.; Huang, L.; Yang, Z.H.; Zhao, F.P. Effects of organic acids on heavy metal release or immobilization in contaminated soil. *Trans. Nonferrous Met. Soc. China* **2022**, *32*, 1277–1289. [CrossRef]

31. Hu, S.W.; Li, H.; Wang, P.; Liu, C.X.; Shi, Z.Q.; Li, F.B.; Liu, T.X. Interfacial photoreactions of Cr(VI) and oxalate on lepidocrocite surface under oxic and acidic conditions: Reaction mechanism and potential implications for contaminant degradation in surface waters. *Chem. Geol.* **2021**, *583*, 120481. [CrossRef]

32. Kitadai, N.; Nishiuchi, K. Thermodynamic impact of mineral surfaces on amino acid polymerization: Aspartate dimerization on goethite. *Astrobiology* **2019**, *19*, 1363–1376. [CrossRef] [PubMed]

33. Lambert, J.F. Adsorption and polymerization of amino acids on mineral surfaces: A review. *Orig. Life Evol. Biosph.* **2008**, *38*, 211–242. [CrossRef] [PubMed]

34. Lee, N.; Sverjensky, D.A.; Hazen, R.M. Cooperative and competitive adsorption of amino acids with Ca^{2+} on rutile (α-TiO$_2$). *Environ. Sci. Technol.* **2014**, *48*, 9358–9365. [CrossRef] [PubMed]

35. Yeasmin, S.; Singh, B.; Kookana, R.S.; Farrell, M.; Sparks, D.L.; Johnston, C.T. Influence of mineral characteristics on the retention of low molecular weight organic compounds: A batch sorption-desorption and ATR-FTIR study. *J. Colloid. Interf. Sci.* **2014**, *432*, 246–257. [CrossRef]

36. Lewis, D.G.; Farmer, V.C. Infrared absorption of surface hydroxyl groups and lattice vibrations in lepidocrocite (γ-FeOOH) and boehmite (γ-AlOOH). *Clay. Miner.* **1986**, *21*, 93–100. [CrossRef]

37. Li, X.F.; Guo, C.L.; Jin, X.H.; He, C.C.; Dang, Z. Mechanisms of Cr(VI) adsorption on schwertmannite under environmental disturbance: Changes in surface complex structures. *J. Hazard. Mater.* **2021**, *416*, 125781. [CrossRef]

38. Jing, L.; Zhu, R.; Liang, X.; Ma, L.; Molinari, M. Synergistic adsorption of Cd(II) with sulfate/phosphate on ferrihydrite: An in situ ATR-FTIR/2D-COS study. *Chem. Geol.* **2018**, *477*, 12–21.

39. Bartlett, R.; James, B. Behavior of Chromium in Soils: III. *Oxidation1. J. Environ. Qual.* **1979**, *8*, 31–35. [CrossRef]

40. Yan, W.; Jing, C.Y. Molecular insights into glyphosate adsorption to goethite gained from ATR-FTIR, two-dimensional correlation spectroscopy, and DFT study. *Environ. Sci. Technol.* **2018**, *52*, 1946. [CrossRef]

41. Noda, I.; Dowrey, A.E.; Ozaki, Y. *Two-Dimensional Correlation Spectroscopy. Applications in Vibrational and Optical Spectroscopy*; John Wiley & Sons, Inc.: Hoboken, NJ, USA, 2004.

42. Christensen, A.N.; Lehmann, M.S.; Convert, P.; Beyer, L.; Cyvin, S.J. Deuteration of crystalline hydroxides. Hydrogen bonds of gamma-AlOO(H,D) and gamma-FeOO(H,D). *Acta Chem. Scand* **1982**, *36*, 303–308. [CrossRef]

43. Song, X.; Boily, J.-F. Structural controls on OH site availability and reactivity at iron oxyhydroxide particle surfaces. *Phys. Chem. Chem. Phys.* **2012**, *14*, 2579–2586. [CrossRef]

44. Li, T.F.; Li, X.F.; Shen, C.R.; Chen, D.; Li, F.H.; Xu, W.C.; Wu, X.L.; Bao, Y.P. Nano-hydroxyapatite modified tobacco stalk-based biochar for immobilizing Cd(II): Interfacial adsorption behavior and mechanisms. *Processes* **2024**, *12*, 1924. [CrossRef]

45. Gan, M.; Sun, S.; Zheng, Z.; Tang, H.; Sheng, J.; Zhu, J.; Liu, X. Adsorption of Cr(VI) and Cu(II) by AlPO$_4$ modified biosynthetic Schwertmannite. *Appl. Surf. Sci.* **2015**, *356*, 986–997. [CrossRef]

46. Wang, X.H.; Liu, F.F.; Lu, L.; Yang, S.; Zhao, Y.; Sun, L.B.; Wang, S.G. Individual and competitive adsorption of Cr(VI) and phosphate onto synthetic Fe-Al hydroxides. *Colloid. Surf. A* **2013**, *423*, 42–49. [CrossRef]

47. Liu, B.X.; Chen, C.; Li, W.; Liu, H.Y.; Liu, L.; Deng, S.S.; Li, Y. Effective removal of Cr(VI) from aqueous solution through adsorption and reduction by magnetic S-doped Fe-Cu-La trimetallic oxides. *J. Environ. Chem. Eng.* **2022**, *10*, 107433. [CrossRef]

48. Johnston, C.P.; Chrysochoou, M. Mechanisms of chromate adsorption on hematite. *Geochim. Cosmochim. Acta* **2014**, *138*, 146–157. [CrossRef]

49. Hoffmann, M.M.; Darab, J.G.; Fulton, J.L. An infrared and X-ray absorption study of the structure and equilibrium of chromate, bichromate, and dichromate in high-temperature aqueous solutions. *J. Phys. Chem. A* **2001**, *105*, 6876–6885. [CrossRef]

50. Parikh, S.J.; Kubicki, J.D.; Jonsson, C.M.; Jonsson, C.L.; Hazen, R.M.; Sverjensky, D.A.; Sparks, D.L. Evaluating glutamate and aspartate binding mechanisms to rutile (α-TiO$_2$) via ATR-FTIR spectroscopy and quantum chemical calculations. *Langmuir* **2011**, *27*, 1778–1787. [CrossRef] [PubMed]

51. Hug, S.J.; Bahnemann, D. Infrared spectra of oxalate, malonate and succinate adsorbed on the aqueous surface of rutile, anatase and lepidocrocite measured with in situ ATR-FTIR. *J. Electron. Spectrosc. Relat. Phenom.* **2006**, *150*, 208–219. [CrossRef]

52. Li, X.F.; Li, T.F.; Jeyakumar, P.; Li, J.Y.; Jin, X.H.; Zhang, J.; Guo, C.L.; Jiang, X.D.; Lu, G.N.; Dang, Z.; et al. Effect of biochar-derived DOM on contrasting redistribution of chromate during Schwertmannite dissolution and recrystallization. *J. Hazard. Mater.* **2024**, *476*, 134988. [CrossRef] [PubMed]

53. Simanova, A.A.; Loring, J.S.; Persson, P. Formation of ternary metal-oxalate surface complexes on α-FeOOH particles. *J. Phys. Chem. C* **2011**, *115*, 21191–21198. [CrossRef]

54. Hay, M.B.; Myneni, S.C.B. Structural environments of carboxyl groups in natural organic molecules from terrestrial systems. Part 1: Infrared spectroscopy. *Geochim. Cosmochim. Acta* **2007**, *71*, 3518–3532. [CrossRef]

55. Langmuir, I. The Adsorption of gases on plane surfaces of glass, mica and platinum. *J. Am. Chem. Soc.* **1918**, *40*, 1361–1403. [CrossRef]

56. Freundlich, H.M.F. Über die adsorption in lösungen Z. *Phys. Chem.* **1906**, *57A*, 385–470. [CrossRef]